The Response of the Large-Scale Tropical Circulation to Warming

Levi G. Silvers[1] , Kevin A. Reed[1] , and Allison A. Wing[2]

[1]School of Marine and Atmospheric Sciences, State University of New York at Stony Brook, Stony Brook, NY, USA, [2]Department of Earth, Ocean, and Atmospheric Science, Florida State University, Tallahassee, FL, USA

Abstract Previous work has found that as the surface warms the large-scale tropical circulations weaken, convective anvil cloud fraction decreases, and atmospheric static stability increases. Circulation changes inevitably lead to changes in the humidity and cloud fields which influence the surface energetics. The exchange of mass between the boundary layer (BL) and the midtroposphere has also been shown to weaken in global climate models. What has remained less clear is how robust these changes in the circulation are to different representations of convection, clouds, and microphysics in numerical models. We use simulations from the Radiative-Convective Equilibrium Model Intercomparison Project to investigate the interaction between overturning circulations, surface temperature, and atmospheric moisture. We analyze the underlying mechanisms of these relationships using a 21-member model ensemble that includes both General Circulation Models and Cloud-system Resolving Models. We find a large spread in the change of intensity of the overturning circulation. Both the range of the circulation intensity, and its change with warming can be explained by the range of the mean upward vertical velocity. There is also a consistent decrease in the exchange of mass between the BL and the midtroposphere. However, the magnitude of the decrease varies substantially due to the range of responses in both mean precipitation and mean precipitable water. We hypothesize based on these results that despite well understood thermodynamic constraints, there is still a considerable ability for the cloud fields and the precipitation efficiency to drive a substantial range of tropical convective responses to warming.

Plain Language Summary Tropical large-scale overturning circulations are expected to weaken with warming. This weakening is the result of precipitation increasing at a slower rate than the atmospheric water vapor. Because precipitation and water vapor are important measures of how energy flows through the atmosphere it is important to understand how they will respond to a warming climate. We use two methods to calculate the change of the overturning circulation in 21 different simulations of the tropical atmosphere. This group of 21 models includes high resolution models that resolve cloud systems, and global models with grid-spacing of about 100 km. We show that a weakening circulation that results from increasing atmospheric stability and increased water vapor is a robust result across most models. But across the group of models there is a large range of magnitudes in the response of the circulation to warming. This variability is well explained by the magnitude of the mean upward vertical velocity. Higher resolution models do not have a narrower range of responses. Narrowing this range of responses will depend on developing a better understanding of what drives the variations in atmospheric stability, surface fluxes of latent energy, and relative humidity.

1. Introduction

Progress has been made in recent work that has contributed to a better understanding of how Earth's climate will respond to increasing concentrations of greenhouse gases (GHG). The expected global mean thermodynamic and hydrologic response to GHG forcing is becoming clearer and the range of anticipated feedback responses to GHG forcing is narrowing (Sherwood et al., 2020). However, predicting and understanding how dynamic circulations, local feedback processes, and regional precipitation characteristics will adjust to changes in the climate remains challenging (Shepherd, 2014; Voigt & Shaw, 2015). The circulation of the atmosphere is a critical determining factor in the location of regional changes to weather and climate, with direct consequences for society. While changes of circulation are predicted to result from the warming of Earth's climate, there is a large range in the circulation patterns and characteristics projected by the current generation of comprehensive global climate models.

Interactions between clouds and the large-scale circulation are particularly important in the tropical regions of Earth. These regions are characterized by large areas of clear-sky subsidence and concentrated towers of convection that often aggregate into persistent cloudy areas where vertical ascent is dominant (Bjerknes, 1938; Riehl & Malkus, 1958). This ascent and the compensating subsidence constitute the large-scale overturning tropical circulation which can manifest as the inter-tropical convergence zone, the Hadley circulation, and the Walker circulation. There is evidence that the large-scale overturning circulation will decrease in strength as the global mean temperature increases. This overturning circulation has been quantified in multiple ways including the mass exchange M (kgm^{-2} s^{-1}) between the boundary layer (BL) and the free troposphere (Betts & Ridgway, 1989; Held & Soden, 2006), a mass streamfunction (kgs^{-1}) (e.g., Randall, 2015), the rate at which water vapor cycles through the atmosphere M_{wv} (s^{-1}) (Bosilovich et al., 2005; Roads et al., 1998), and the intensity of the circulation (I) as measured using the mid-tropospheric pressure velocity (Bony et al., 2013; Cronin & Wing, 2017; Medeiros et al., 2015). A mass streamfunction provides an elegant representation of the mean meridional circulation on Earth. But the application of this approach, which often relies on geographically oriented axes, is less intuitive with simulations of radiative convective equilibrium (RCE) in which there is no inherent distinction between the axes. Unlike Earth where the tropics present a perpetual source of excess energy that is transported meridionally, RCE simulations are dominated by numerous clusters of convection which often form and propagate in arbitrary locations and directions. Interestingly, the physical reasoning for a decrease in circulation strength differs between M and I. A decrease of M can be inferred from the relationship $P = Mq$ in which P (kgm^{-2} s^{-1}) is the mean precipitation and q is the BL mixing ratio. Although there is substantial scatter among models and observations, the change of precipitation with warming is often assumed to be around 2–3%K^{-1} and significantly less than the change of q which scales with the Clausius-Clapeyron (CC) relation (Betts & Ridgway, 1989; Held & Soden, 2006; Jeevanjee & Romps, 2018). In contrast, a decreasing intensity of the circulation, I, is closely connected to the enhanced net radiative cooling and the increased static stability that result from a warmer climate (Bony et al., 2013, 2016; Knutson & Manabe, 1995). This picture of warming-induced changes that include a weakening tropical circulation and subsidence velocity along with an increasing static stability and residence time of water vapor has become fairly clear in the literature of recent decades (e.g., Jenney et al., 2020).

However, important questions remain. For example, how robustly do models of RCE represent these warming induced changes to the circulation? How does the circulation response to warming in RCE simulations compare between General Circulation Models (GCMs) and Cloud-system Resolving Models (CRMs) despite the large difference in grid-spacing of the two model types? Many previous studies have looked at overturning circulations in observations or in GCMs in which the circulations are clearly linked to large-scale temperature gradients, spatial differences in the insolation, and the rotation of Earth (e.g., Held & Soden, 2006; Medeiros et al., 2015; Vecchi & Soden, 2007). The large-scale circulations of RCE simulations are driven not by external factors like large-scale gradients in the temperature at the surface or in the insolation. Instead, feedback mechanisms between convection and its surrounding environment drive a mean ascent in coherent regions of convection and radiatively-driven subsidence in the surrounding clear-sky regions and in many cases allow for the self-aggregation of convection (Wing et al., 2017).

The relation between Earth's observed tropical large-scale circulation and circulations that are generated in RCE simulations is not obvious a priori. A common metric of the large-scale circulation is the vertical pressure velocity on the 500 hPa pressure surface (ω_{500}). Remarkably, the probability distribution function of ω_{500} is similar among RCE simulations, Aquaplanet simulations, *amip* simulations, and reanalyzes that are heavily dependent on observations (Bony et al., 2004; Cronin & Wing, 2017; Medeiros et al., 2015). The similarity is due not primarily to the regions of deep convection, but rather to subsiding regions of the tropics where the dominant statistical weight of moderately subsiding air ($\approx$10–20 hPa day^{-1}) indicates large regions with favorable conditions for shallow BL clouds. This rate of subsidence is largely constrained by the clear-sky radiative cooling rate and provides evidence that the distribution of the large-scale dynamic regimes in the tropics are driven partly by the energetics of clear-sky regions. The similarity of dynamic regimes encourages further research into the physical mechanisms and coupling processes between clouds and the circulation that could be shared among the observed atmosphere, Earth-like simulations, and various models of RCE.

This study focuses on the intensity, and the change of intensity with warming, of the large-scale circulation that is created entirely by the interactions between atmospheric radiation and convection across a large range of models that participated in the Radiative-Convective Equilibrium Model Intercomparison Project (RCEMIP; Wing et al., 2018). One of the goals of this work is to provide context for future studies of the tropical overturning

Table 1
List of Models That Are Used in This Study and That Participated in RCEMIP

Model abbreviation	Model name	Model type	Color
CAM5-GCM	Community Atmosphere Model v5	GCM	◼
CAM6-GCM	Community Atmosphere Model v6	GCM	◼
CNRM-CM6-1	Atmospheric component of the CNRM Climate Model 6.1	GCM	◼
ECHAM6-GCM	MPI-M Earth System Model-Atmosphere component v6.3.04p1	GCM	◼
GEOS-GCM	Goddard Earth Observing System model v5.21	GCM	◼
ICON-GCM	ICOsahedral Nonhydrostatic Earth System Model-Atmosphere component	GCM	◼
SAM0-UNICON	Seoul National University Atmosphere Model v0	GCM	◼
SP-CAM	Super-Parameterized Community Atmosphere Model	GCM	◼
SPX-CAM	Multi-instance Super-Parameterized CAM	GCM	◼
UKMO-GA7.1	UK Met Office Unified Model Global Atmosphere v7.1	GCM	◼
ICON-LEM	ICOsahedral Nonhydrostatic-2.3.00, LEM	CRM	◼
ICON-NWP	ICOsahedral Nonhydrostatic-2.3.00, NWP	CRM	◼
MESONH	Meso-NH v5.4.1	CRM	◼
SAM-CRM	System for Atmospheric Modeling 6.11.2	CRM	◼
SCALE	SCALE v5.2.5	CRM	◼
UCLA-CRM	UCLA Large-Eddy Simulation model	CRM	◼
UKMO-CASIM	UK Met Office Idealized Model v11.0 - CASIM	CRM	◼
UKMO-RA1-T	UK Met Office Idealized Model v11.0 - RA1-T	CRM	◼
UKMO-RA1-T-nocloud	UK Met Office Idealized Model v11.0 - RA1-T	CRM	◼
WRF-COL-CRM	Weather Research and Forecasting model v3.5.1	CRM	◼
WRF-CRM	Weather Research and Forecasting model v3.9.1	CRM	◼

Note. The colors used to identify models are the same as those used in Wing et al. (2020).

circulation when forced either by idealized sea surface temperature (SST) patterns that generate a mock-Walker circulation (e.g., Bretherton & Sobel, 2002; Grabowski et al., 2000; Lutsko & Cronin, 2018; Raymond, 1994; Silvers & Robinson, 2021; Tompkins, 2001) or by observed Earth-like conditions (Vecchi & Soden, 2007). Although an idealization, RCE resembles the deep tropics of Earth where there is little of the horizontal energy advection that can dominate the energetics of higher latitudes. Our analysis is driven largely by these two questions:

1. How does the overturning circulation change with warming in the RCEMIP multi-model ensemble?
2. What controls the intermodel spread in the circulation strength and the change with warming?

The remainder of this paper is organized as follows. The RCEMIP configurations, experiments used, and analysis methods are described in Section 2. Section 3 calculates the change of circulation with warming. This is done with two different methods, and the connection between the methods is discussed. In Section 4 we illustrate some of the sources of intermodel spread. This includes Section 4.1 which discusses the role of the surface energy flux and precipitation on the overturning circulation and Section 4.2 which illustrates the range of variability of the static stability and relative humidity. The main conclusions and final comments are presented in Section 5.

2. Experiments and Methods

All experiments used in this paper follow the RCEMIP protocol and experiments documented by Wing et al. (2018, 2020). Throughout this paper we have used the same colors and model abbreviations to identify models as in Wing et al. (2020) and as shown in Table 1. A brief description of the experiments follows. RCE is simulated for three prescribed SST (represented as T_s in this paper) values, 295, 300, and 305 K. There is no rotation or land surface, no imposed circulation or dynamic forcing, and the insolation is uniform at every grid-point

(409.6 W m^{-2}). The RCE simulations (RCE_large) were initialized from mean soundings of equilibrated RCE simulations on smaller domains (RCE_small) for CRMs. The initial conditions for the RCE_small simulations were generated from an approximation of a moist tropical sounding (Wing et al., 2018). There are no aerosol radiative effects. Much of the previous work that discusses the change of overturning circulations with warming (e.g., Bony & Stevens, 2020; Held & Soden, 2006; Vecchi & Soden, 2007) discuss the role of increasing concentrations of CO_2 in reducing the radiative cooling rates. It is important to note that for the RCEMIP experiments studied in this paper the warming is entirely due to increased T_s with no change in the CO_2 concentration. There is no impact from changing CO_2 concentrations on the atmospheric cooling rates in our simulations.

We have analyzed data from 21 of the models that participated in RCEMIP. Descriptions of the models and further details and analysis can be found in Wing et al. (2020) and Appendix A. Unless noted otherwise, values from GCMs will be displayed with circles and values from CRMs will be displayed with stars. The RCEMIP simulations with prescribed T_s of 295, 300, and 305 K are distinguished with increasing marker size. RCEMIP data is publicly available at http://hdl.handle.net/21.14101/d4beee8e-6996-453e-bbd1-ff53b6874c0e where it is hosted by the German Climate Computing Center (Deutsches Klimarechenzentrum, DKRZ).

Multiple domain configurations were used by CRMs as part of RCEMIP. Our analysis focuses on the RCE_large domain configuration for CRMs and the global domain for GCMs. The CRM RCE_large domain is a doubly periodic channel with horizontal dimensions of ∼6, 000 × 400 km^2, a model top at ∼33 km, and a recommendation of using 74 vertical levels. All of the CRMs used a horizontal grid-spacing of 3 km. The GCMs use a horizontal grid-spacing similar to the configuration used by each model for CMIP6 in which ∼100 km is typical. In order to focus on the large scale circulations and to consistently compare the CRMs and GCMs, we have coarsened the CRMs to a grid with blocks that are 96 × 96 km^2 and all GCM data is interpolated to a 1° latitude-longitude grid. Chunks of 5 days were averaged before computing I, $\omega^\downarrow$, or $\omega^\uparrow$. Domain mean vertical profiles of relative humidity and temperature have been used in Section 4 and for the calculation of the diabatic velocity and the static stability. For the CRM simulations these profiles are averages over the last 25 days of the simulations. The experiments using CRMs simulated 100 days, and the last 50 days have been analyzed. The experiments that used the GCMs simulated at least 1,000 days, and for this paper we have analyzed the last year of the simulations. Additional details of model configurations are given in Appendix A.

3. Changes of Circulation

Changes in the vertical circulation in the tropics due to warming can be quantified in various ways. Held and Soden (2006) showed that the exchange of mass M between the BL and the free troposphere is a useful measure. This constrains M based on the precipitation and the BL mixing ratio. Alternatively, the intensity of the overturning dynamic circulation, I, in the mid-troposphere can be examined using the mean ascending and descending velocities, as in Bony et al. (2013). In the following two subsections we use these measures of the tropical circulation along with M_{wv} to show how the hydrologic cycle and the large-scale circulation change as the surface warms.

3.1. Water Vapor Cycling and Circulation

The CC relation provides a constraint on the change of the saturation vapor pressure with temperature. Because of this constraint we anticipate an increasing column-integrated water vapor, or precipitable water (PW), PW (kg m^{-2}), with increasing surface temperature T_s. All of the RCEMIP models we analyze show an increase of PW with T_s (Figure 1a). The range of PW across the RCEMIP models for particular T_s values is large (∼12, 16, and 22 kg m^{-2} for 295, 300, 305 K, respectively) and likely indicates different values of surface relative humidity and varying vertical distributions of water vapor. For reference, an analytic function is plotted (black lines) that shows the CC-expected increase of PW as a function of T_s. The three black lines show three particular parameter values that correspond to distinct ratios of the surface relative humidity and the scale height of water vapor (see Appendix B for details, following Stephens (1990)). Although all models show an increase in PW with warming, the range of values at a given T_s and the rate of increase of PW vary widely across models.

Following O'Gorman and Muller (2010), we define the differential change of P as $\delta P = \log{(1 + r_\Delta \Delta T_s)}/\Delta T_s$ with $r_\Delta = (P_2 - P_1)/(P_1 \Delta T_s)$ where the subscripts 1 and 2 indicate simulations at T_s of 295 and 305 K respectively and ΔT_s is 10 K. Differential changes of PW are defined analogously. Previous studies have demonstrated that changes of P in warming experiments, sometimes referred to as the strength of the hydrologic cycle, do not scale with CC
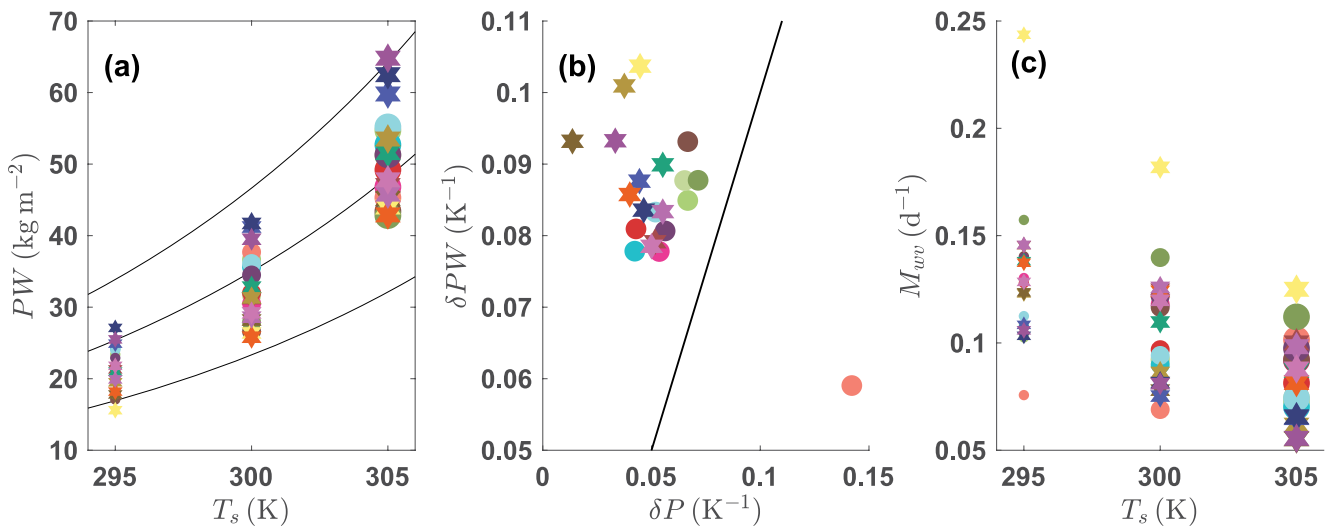
Figure 1. (a) Precipitable water (PW) as a function of T_s, (b) the differential change of PW and P between the T_s 295 and 305 K experiments, (c) and the water vapor cycling rate, M_{wv}, as a function of T_s. General Circulation Models are represented by circles and Cloud-system Resolving Models by stars, increasing marker size indicates increasing values of T_s. Colors represent individual models, as given in Table 1. The 1:1 slope is plotted in (b) for reference.

but increases at a slower rate (e.g., Allen & Ingram, 2002; Boer, 1993; Flaschner et al., 2016). We find that the change of P with warming is larger than expected based on previous studies (Held & Soden, 2006), but is still smaller than the CC scaling that dominates changes of PW (Figure 1b). It is worth noting that the CRMs show a smaller range of change in P with a mean value of 4.8% K^{-1}. The mean rate of change of PW (8.5% K^{-1}) is larger than the value often stated for CC scaling (6.5 − 7% K^{-1}). However, O'Gorman and Muller (2010) showed that the differential change in PW varies strongly in latitude and that tropical values are often between 8 and 9% K^{-1}, consistent with our findings from RCEMIP.

The mean precipitation, P, is not constrained by CC, but rather by the net radiative cooling of the atmosphere. Jeevanjee and Romps (2018) provide an elegant explanation for an increase of P of approximately 2%–3% K^{-1} that made use of clear-sky radiative fluxes. When discussing the radiative constraint on changes of mean P, numerous studies assume that RH is relatively constant with surface warming (Held & Soden, 2006), and that the profiles of mean RH are invariant when plotted in temperature space (Jeevanjee & Romps, 2018; Romps, 2014). Our findings are consistent in the sense that RH changes substantially less with warming than does the specific humidity, and RH profiles have less variation with warming when plotted in temperature coordinates than they do in pressure or height coordinates (Stauffer & Wing, 2022). However, these approximations hold to varying degrees across the RCEMIP multi-model ensemble. We find a larger range in the change of P than did previous studies such as Held and Soden (2006), larger cloud fractions in most RCE models relative to the model used in Romps (2014) and Jeevanjee and Romps (2018), and a large range of RH profiles (see Wing et al. (2020); Stauffer and Wing (2022) and Section 4.2.). Our interpretation is that the overall picture of the radiative constraint on changes in mean P that has been expounded in such studies as Held and Soden (2006) and Jeevanjee and Romps (2018) is correct, but that variations from this picture can be substantial and are likely due to the structure of clouds, the precipitation efficiency, and the relative humidity of the troposphere. As previously mentioned, the change in the upward mass flux from a convective BL is determined by the ratio of the change in P and the change in the mixing ratio of specific humidity. In the RCEMIP models examined here, the mean rate of change of P (5.4% K^{-1}) is substantially less than that of the PW (8.5% K^{-1}) although P and PW show considerable spread in both GCMs and CRMs (Figure 1b). This implies that in all but one of the RCEMIP models, M decreases as T_s increases.

Closely related to M is the cycling rate of water vapor, here defined as $M_{wv} = P/PW$. M_{wv} can also be thought of as the inverse "residence time" of water vapor. As the surface warms, water vapor stays in the troposphere longer and M_{wv} decreases (Figure 1c). For example, with a T_s of 295 K, the UCLA-CRM model has a residence time (1/M_{wv}) of water vapor in the troposphere of about 4 days which increases to 7.7 days in the simulation with a T_s of 305 K. Over the same change of T_s the residence time of the CAM5-GCM model increases from 10 to 14.3 days.
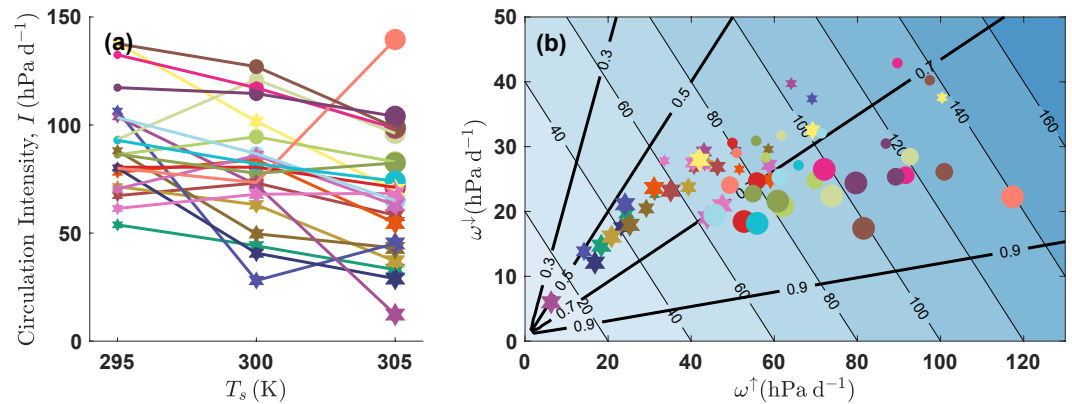
Figure 2. (a) Intensity of the large-scale circulation, I, as a function of T_s. (b) Intensity of large-scale circulation (shading, hPa d^{-1}) decomposed into the magnitude of individual components $\omega^{\downarrow}$ and $\omega^{\uparrow}$. Thick black lines represent constant values of the subsidence fraction (0.3, 0.5, 0.7, and 0.9). Circles (stars) indicate General Circulation Models (GCMs) (Cloud-system Resolving Models (CRMs)) and increasing marker size indicates increased values of T_s. All GCMs have been interpolated to a 1×1 degree grid and the CRMs have been coarsened to blocks that are $(96 \ km)^2$.

As the rate of mass exchange (M) between the BL and the free-troposphere decreases, the residence time of water vapor increases. The range of M_{wv} values across the RCEMIP models is large [0.08:0.24] at 295 K and [0.06:0.13] at 305 K; Figure 1c. Of the 21 models examined, 20 have $\delta PW > \delta P$ (Figure 1b) and as a result, M and M_{wv} decrease with surface warming in those models (Figure 1c). The one model for which $\delta P > \delta PW$ has an increase of M_{wv} and is thus still consistent with the scaling of Betts and Ridgway (1989) and Held and Soden (2006). This scaling relies on the assumption that the distribution of relative humidity will not greatly change as the surface warms. Interestingly, the one model that shows an increase of M_{wv} also shows a large change of the relative humidity with warming in the 305 K simulation. Despite the basic physics that is encapsulated by the CC relation and the balance between P and the net radiative cooling, the RCEMIP models still contain enough degrees of freedom to generate a diverse range of responses to the RCEMIP boundary conditions.

3.2. Intensity of the Mid-Tropospheric Overturning Circulation

An alternative to the thermodynamically driven cycling rate of water vapor, M_{wv}, is to calculate the intensity of the large-scale overturning circulation as $I = \omega^{\downarrow} - \omega^{\uparrow}$, where $\omega^{\uparrow}$ is the mean upward vertical velocity and $\omega^{\downarrow}$ is the mean downward vertical velocity in the mid-troposphere as approximated on the 500 hPa pressure surface (Bony et al., 2013; Medeiros et al., 2015). In contrast to M and M_{wv}, I directly ties the overturning circulation to the dynamics of the troposphere. Defining the overturning circulation in this way also makes a connection to the subsidence fraction (SF; fraction of domain with subsiding motion at 500 hPa), which is often used as a metric that indicates the degree of convective self-aggregation, or clustering, that is present in an experiment (e.g., Coppin & Bony, 2015; Cronin & Wing, 2017; Wing et al., 2020). Assuming continuity allows one to write an expression for I in terms of SF, $\omega^{\downarrow}$, and $\omega^{\uparrow}$:

$$I = \frac{1}{1 - SF}\omega^{\downarrow} = -\frac{1}{SF}\omega^{\uparrow}. \qquad (1)$$

For the majority of models the circulation intensity I decreases with warming (Figure 2a). As is clear from Equation 1 and discussed by Cronin and Wing (2017), if the SF is constant then both the magnitude and change of I are linearly related to the magnitude and change of $\omega^{\uparrow}$ and $\omega^{\downarrow}$. To examine this in the context of the RCEMIP models Figure 2b plots the circulation intensity (shading) for each simulation according to each component, $\omega^{\uparrow}$ and $\omega^{\downarrow}$. We have also used Equation 1 to plot constant SF values of 0.3, 0.5, 0.7, and 0.9 and illustrate the relationship between I, $\omega^{\uparrow}$, and $\omega^{\downarrow}$. Several characteristics of the solutions are apparent. The SF of individual simulations is greater than or equal to 0.5, implying that the convective heating is larger than the radiative cooling (Jenney et al., 2020). The CRMs (stars) tend to have smaller values of I and SF. For the GCM simulations, the solutions often equilibrate with larger values of SF as T_s is increased. The varying degrees of self-aggregation that are typical for large domain RCE simulations are reflected in the scatter of values between the lines of constant SF
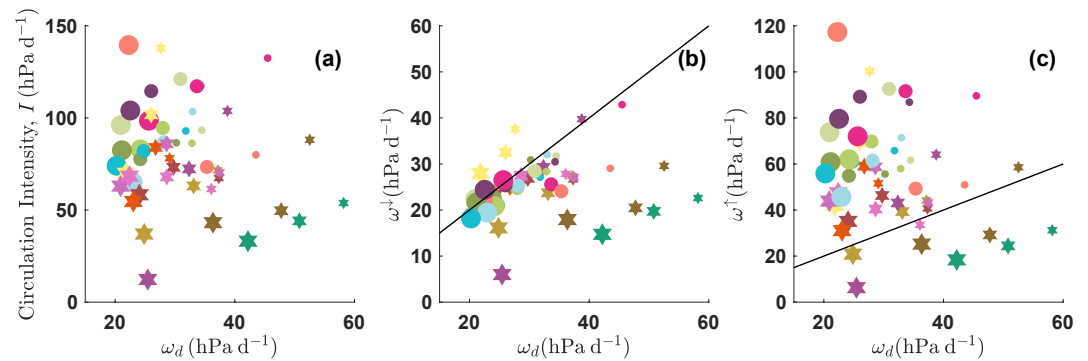
Figure 3. (a) Relationship between I and the diabatically driven subsidence velocity, ω_d. (b) Relationship between $\omega^\downarrow$ and ω_d. (c) Relationship between the $\omega^\uparrow$ and ω_d. Diabatic velocity values have been computed as the mass weighted mean between 200 and 600 hPa. Circles (stars) indicate General Circulation Models (Cloud-system Resolving Models) and increasing marker size indicates increases values of T_s. For reference black lines show a 1:1 slope. The ω_d has only been computed for models which provided clear-sky radiative fluxes.

of 0.5 and 0.9 (Figure 2b). Although the wide range of values in I correspond closely to the wide range of values of $\omega^\uparrow$, to the extent that SF is constant, the intensity of the circulation I can be linearly scaled by either $\omega^\uparrow$ or $\omega^\downarrow$ (Equation 1).

Both observations and theory indicate that the preferred state of the tropical atmosphere is one that maintains broad weakly subsiding regions punctuated by narrow towers of relatively strong ascent (Bjerknes, 1938). The consistency with which $\omega^\uparrow > \omega^\downarrow$ in Figure 2b confirms this tendency among the RCEMIP models. There is a wide range in the values of $\omega^\uparrow/\omega^\downarrow$ with many of the CRMs having almost the same values of mean upward and downward velocity while the GCMs in some cases have values of $\omega^\uparrow$ that are 3–4 larger than $\omega^\downarrow$.

In the tropics, the mean vertical velocity in the subsidence regions is often (Bony et al., 2016; Cronin & Wing, 2017; Larson et al., 1999; Mapes, 2001) approximated by the so-called diabatic velocity, ω_d, sometimes referred to as the radiative-subsidence velocity. We are interested in comparing ω_d with the mean subsidence velocities, $\omega^\downarrow$, that are simulated by the RCEMIP models. Formally ω_d can be derived from the dry static energy budget equation. Assuming a steady-state tropical-like environment in which the horizontal advection of temperature is negligible reduces the budget equation to

$$\omega_d \approx Q/\sigma, \tag{2}$$

in which Q is the radiative heating or cooling from diabatic processes and σ is the static stability given by
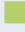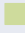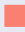
$$\sigma = \frac{\partial s/C_p}{\partial p}, \tag{3}$$

with s the dry static energy, p pressure, and C_p the heat capacity at constant pressure. The balance given by Equation 2 has been utilized and discussed in numerous studies that draw on the theory presented by Charney (1963) and Sobel et al. (2001) (e.g., Bony et al., 2016; Jenney et al., 2020; Larson et al., 1999; Mapes, 2001; Thompson et al., 2017). In regions of ascent, the heating is due largely to condensational processes and in subsidence regions it is dominated by the atmospheric radiative cooling. The most accurate calculation of ω_d would use the total diabatic heating sampled from regions of subsidence. However, for this study we assume that the diabatic heating from regions of subsidence can be approximated by the domain mean clear-sky radiative cooling. This approximation for Q is practical as in aggregated convection, the domain mean is dominated by the subsidence regions, the mean clear-sky radiative cooling rates are often standard GCM output, and 3D data of total diabatic cooling rates from simulations are often not available. Note that because the SF is greater than 0.5, the subsiding regions will naturally have a larger statistical weight in the domain mean cooling rates than do the regions of ascent. The use of the clear-sky radiative cooling for Q has become somewhat standard in both theoretical work and in the evaluation of models (Bony et al., 2016; Cronin & Wing, 2017; Emanuel, 2019; Mapes, 2001; Stauffer & Wing, 2022).

As T_s increases, both I and ω_d decrease for most models (Figure 3a). However, the relationship between I and ω_d for specific models varies widely. We are interested in the relationship between ω_d and each of I, $\omega^\uparrow$, and $\omega^\downarrow$. Scatter plots of $\omega^\downarrow$ (Figure 3b) and $\omega^\uparrow$ (Figure 3c) compared to ω_d reveal a tight relationship between $\omega^\downarrow$ and ω_d. This

Table 2
Correlation Coefficients From the Three T_s Simulations Between I and $\omega^\uparrow$, I and $\omega^\downarrow$, I and ω_d, ω_d and $\omega^\uparrow$, and ω_d and $\omega^\downarrow$

Model		$I, \omega^\uparrow$	$I, \omega^\downarrow$	I, ω_d	$\omega_d, \omega^\uparrow$	$\omega_d, \omega^\downarrow$
CAM5-GCM		**0.81**	0.31	0.21	-0.41	**0.99**
CAM6-GCM		**0.95**	0.08	0.17	-0.13	**1.0**
CNRM-CM6-1		**0.85**	**0.81**	**0.99**	**0.75**	**0.90**
ECHAM6-GCM		0.03	**0.87**	-	-	-
GEOS-GCM		**1.0**	-0.64	**-0.89**	**-0.92**	**0.92**
ICON-GCM		**0.91**	**0.92**	-	-	-
SAM0-UNICON		0.16	**0.77**	0.61	-0.68	**0.98**
SP-CAM		**1.0**	**0.99**	**1.0**	**0.99**	**1.0**
SPX-CAM		**0.99**	**0.99**	**1.0**	**0.99**	**1.0**
UKMO-GA7.1		**0.91**	**0.76**	**0.85**	0.55	**0.99**
ICON-LEM		**1.0**	**1.0**	**1.0**	**0.99**	**1.0**
ICON-NWP		**1.0**	**1.0**	**0.81**	**0.80**	**0.85**
MESONH		**1.0**	0.72	**0.83**	**0.79**	**0.98**
SAM-CRM		**0.99**	**0.94**	0.54	0.43	**0.79**
SCALE		**1.0**	**0.99**	**1.0**	**1.0**	**0.99**
UCLA-CRM		**1.0**	**1.0**	**0.96**	**0.96**	**0.96**
UKMO-CASIM		**1.0**	**1.0**	**0.99**	**0.99**	**0.98**
UKMO-RA1-T		**0.94**	**0.75**	0.28	-0.07	**0.84**
UKMO-RA1-T-nocloud		**0.89**	-0.57	**-0.91**	**-1.0**	**0.86**
WRF-COL-CRM		**1.0**	**1.0**	-	-	-
WRF-CRM		**1.0**	**1.0**	-	-	-

Note. Absolute values larger than 0.74 have bold text. The ω_d has only been computed for models which provided clear-sky radiative fluxes. GCMs are separated from CRMs by a horizontal line.

relationship falls near the 1:1 line for most of the GCMs. The discrepancy between $\omega^\downarrow$ and ω_d with several of the CRMs in Figure 3b is surprising. With some, although not all, of the CRMs (SCALE, ICON-LEM, ICON-NWP) the agreement improves when $\omega^\downarrow$ is calculated using smaller block sizes. We have also calculated ω_d in the CRMs using the all-sky radiative cooling in subsidence regions. For several of the models (SCALE, ICON-LEM, and ICON-NWP) the resulting values of ω_d decrease in magnitude, bringing them in closer agreement to the values of $\omega^\downarrow$. However, with other models (UCLA-CRM and MESONH) the agreement between ω_d and $\omega^\downarrow$ is worse when ω_d is calculated from the radiative cooling in subsidence regions. The multi-model scatter among values of $\omega^\uparrow$ and ω_d (Figure 3c) is much broader (relative to $\omega^\downarrow$ and ω_d) but several of the individual models show a roughly linear relationship between $\omega^\uparrow$ and ω_d. Overall the general relationships shown here between ω_d, I, $\omega^\downarrow$, and $\omega^\uparrow$ do not change when the mean clear-sky radiative cooling is used for Q versus the total radiative cooling from the subsiding regions. The high correlations between ω_d and $\omega^\downarrow$ (Table 2) and the approximately linear relationships between ω_d, I, $\omega^\downarrow$, and $\omega^\uparrow$ that are seen for individual models in Figure 3 confirm that calculating ω_d with the clear-sky cooling is useful, but the particular relationship between ω_d and $\omega^\downarrow$ is model dependent.

We now illustrate how the variability of I and the change of I with warming compares to the variability of $\omega^\uparrow$, $\omega^\downarrow$, ω_d, and their changes with warming. Correlation calculations confirm several of the visual impressions from Figures 1–3. Although correlations among sets of three points must be cautiously interpreted, they can be helpful to loosely quantify the relationships. For each model we have calculated the correlations of five relationships: I and
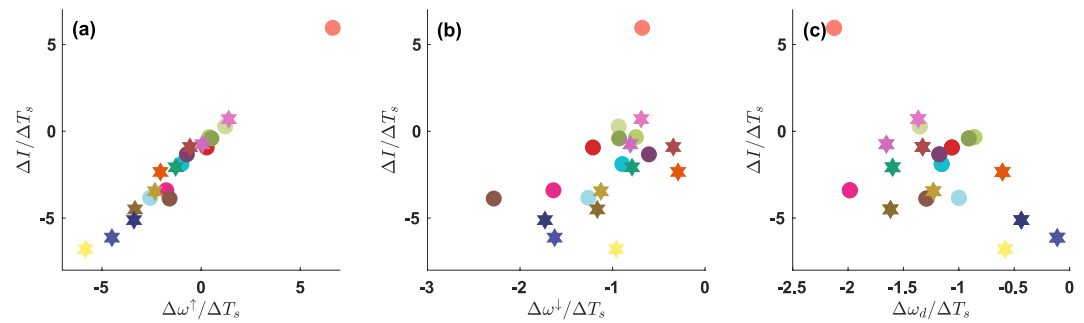
Figure 4. Rates of change with warming (hPa day^{-1} K^{-1}). (a) Rate of change of I compared to the rate of change of $\omega^{\uparrow}$. (b) Rate of change of I compared to the rate of change of $\omega^{\downarrow}$. (c) Rate of change of I compared to the rate of change of ω_d. Circles (stars) indicate General Circulation Models (Cloud-system Resolving Models). Rates have been computed from the best fit polynomial. Correlation coefficients across the ensemble of models are 0.98 (a), 0.67 (b), and -0.47 (c).

$\omega^{\uparrow}$, I and $\omega^{\downarrow}$, I and ω_d, ω_d and $\omega^{\uparrow}$, and ω_d and $\omega^{\downarrow}$. The values are shown in Table 2. The largest multi-model correlations (mean of correlations across models) are between ω_d and $\omega^{\downarrow}$ at 0.94 and between I and $\omega^{\uparrow}$ at 0.88. I also has a relatively high correlation with $\omega^{\downarrow}$ of 0.70. The large range of I is very well explained by the range of $\omega^{\uparrow}$ values. Not only does I have a large range of mean values ($44 - 120$ hPa day^{-1}), the rate of change with warming of I also varies widely from slightly positive to strongly negative (Figure 2). Similar to the range of values of I, the range of values for the slope of I is best explained by the rate of change of $\omega^{\uparrow}$ (Figure 4a). While Figure 4 clearly shows a relationship between $\Delta I/\Delta T_s$, $\Delta\omega^{\downarrow}/\Delta T_s$ and $\Delta\omega_d/\Delta T_s$, the strong linear relation between $\Delta I/\Delta T_s$ and $\Delta\omega^{\uparrow}/\Delta T_s$ is striking and confirms the dominant impact that $\omega^{\uparrow}$ and $\Delta\omega^{\uparrow}/\Delta T_s$ have on I and $\Delta I/\Delta T_s$. The large range of changes in I with warming are much better explained by the changes in the mean upward velocity then by the mean subsidence or radiative velocities. This is consistent with recent work that highlights the important role of changes in the ascending regions of the tropics to the strength of the overturning circulation (Jenney et al., 2020; Mackie & Byrne, 2021).

Both of the measures of tropical circulation discussed thus far show a decreasing strength of circulation as T_s increases for the majority of models, but with a large range of magnitudes. We now briefly examine to what extent these measures are related to each other. Figure 5 shows a scatter plot of the fractional rate of change with warming of I compared to the fractional rate of change of M_{wv}. One feature of Figure 5 that stands out is the fairly tight constraint on the $\Delta M_{wv}/M_{wv}$ near -0.04 for 9 out of 11 CRMs. Several of the GCMs also cluster near this value but overall there is a broader range of possibilities among the GCMs. In contrast to the clustering of the fractional rate of change of M_{wv} around -0.04, the fractional rate of change of I is not constrained in sign and extends over a much wider range. Because the intensity of the circulation, I, is a function of the subsidence fraction, SF, the large range of both I and $\Delta I/\Delta T_s$ reflect a broad diversity of organized convection and subsidence regions (see, e.g., Figure 4 of Wing et al., 2020). In contrast, we do not expect M_{wv} to be directly influenced by the structure of the convective regions but rather by thermodynamic and energetic balances. M_{wv} is constrained by both the net atmospheric cooling and the CC relation. Of central importance to the energetic flux that precipitation represents is the net atmospheric cooling, Q, which helps to set the value of ω_d. We hypothesize that the tighter constraint on the value of $\Delta M_{wv}/M_{wv}$ that is apparent in Figure 5 reflects the smaller range of variability that is present in the subsiding, clear-sky regions of the troposphere compared to the regions of ascent. This is reflected in the small range of variability of $\omega^{\downarrow}$ and ω_d (relative to $\omega^{\uparrow}$), the high correlation (0.94) between them (Table 2, Figure 3), and by the smaller range of changes with warming of both $\omega^{\downarrow}$ and ω_d (Figure 4).
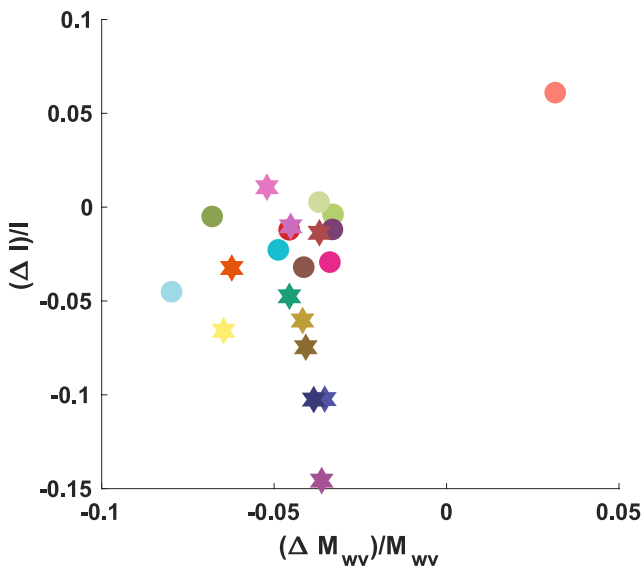
Figure 5. Fractional change of I (hPa day^{-1} K^{-1}) compared to fractional change of the water vapor cycling rate M_{wv} (hPa day^{-1} K^{-1}). The change is computed over the 10 K difference between the three radiative convective equilibrium simulations. Circles (stars) indicate General Circulation Models (Cloud-system Resolving Models).

4. Intermodel Spread of the Overturning Circulation

The previous section showed that both the hydrologic circulation ($M_{wv} \sim P/PW$) and the mean, dynamic overturning circulation (I) decrease with
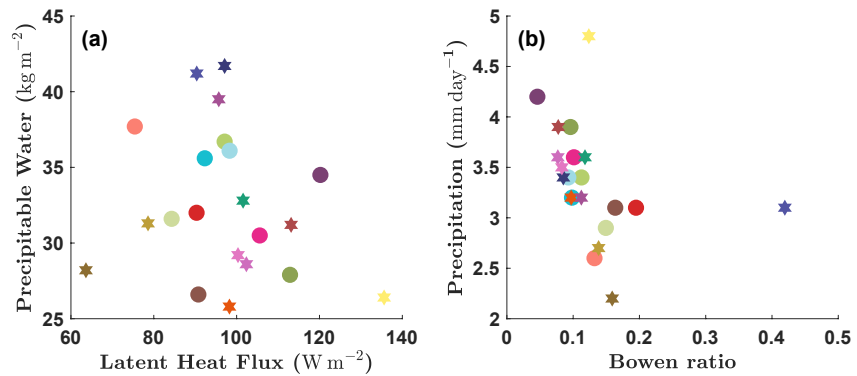
Figure 6. (a) Precipitable Water, *PW*, as a function of the Latent Heat Flux and (b) Precipitation, *P*, as a function of the Bowen ratio for the 300 K simulations. Circles (stars) indicate General Circulation Models (Cloud-system Resolving Models).

warming for the majority of the RCEMIP models. The large intermodel spread of *I* is more accurately mirrored in the spread of $\omega^{\uparrow}$ than $\omega^{\downarrow}$. It was also demonstrated that $\Delta\omega^{\uparrow}/\Delta T_s$ has a much higher correlation with $\Delta I/\Delta T_s$, than does $\Delta\omega^{\downarrow}/\Delta T_s$ (Figure 4). We would like to better understand the source of the wide range of circulation magnitudes shown in Figures 1 and 2. In Section 4.1 the surface energy budget is discussed. The surface energy budget is important for the range of magnitudes in the hydrologic circulation, M_{wv}, and we hypothesize, but do not prove, that it is also important in the range of values of $\omega^{\uparrow}$. Because of their anticipated role in driving variability in the convection (and therefore $\omega^{\uparrow}$ and *I*), in Section 4.2 we look at the relationship of the variability in σ and the net radiative cooling, *Q*, to the diabatic velocity, ω_d, as well as the possible sources of variability in *RH*.

4.1. The Surface Energy Flux and Precipitation

The flux of energy from the surface into the atmosphere is a critical component of the tropical atmospheric circulation and its response to warming. The surface energy budget drives the depth of the atmospheric BL which in turn influences the BL humidity and plays a role in the presence of low-level clouds and their response to a warming surface (Rieck et al., 2012). The surface energy fluxes are also important for the temperature and humidity which determine the low level moist static energy. This moist static energy serves as the fuel that triggers deep convective motions which in turn set the tropospheric temperature, generate anvil cloud, and can amplify the deep overturning circulation.

Any hope that the RCE configuration with a prescribed and uniform T_s, uniform insolation, and a consistent surface albedo would lead to similar surface energy fluxes among the RCEMIP models must be abandoned after a cursory look at the data. The latent heat flux and the resulting *P* differ among the models by up to a factor of 2 (Figure 6), and *PW* varies by almost as much. The domain mean precipitation, *P*, is shown in Figure 6b to vary between about 2.5 mm day^{-1} and 4.5 mm day^{-1}. The range of the Bowen Ratio (ratio of the sensible to latent heat flux) covers more than a factor of two with most of the variations coming from the latent, rather than sensible, heat flux (with the exception of one model). Given the rather tight constraints that are specified in the RCEMIP protocol, what are the likely sources of this large inter-model range? Differences among the incoming solar and longwave radiation at the surface will have very little impact on the surface energetics because of the fixed T_s and the low albedo of water. As long as the overlying atmosphere remains well coupled to the surface the sensible heat flux does not vary much among models because of the fixed T_s. However, the latent heat flux can and does vary widely across the model ensemble with a range of 64, 72, and 87 W m^{-2} for the 295, 300, and 305 K simulations, respectively. The factors that determine how tightly coupled the atmosphere will be to the surface, and consequently what the low-level temperature and humidity will be are critical for determining the sensible and latent heat fluxes. Variations of the low-level temperature and humidity fields, and especially the strong variability of the latent heat flux, will drive a large part of the resulting low-level clouds, the triggering of deep convection, and the variations of *P* among the models. For RCE models using bulk aerodynamic surface flux equations the coupling likely comes down to either the low-level winds or the bulk transfer coefficients.

Among the RCEMIP models, for a particular T_s, M_{wv} varies by more than a factor of two. This variability is driven by a large range of values in both *P* and *PW*. We know that *P* is tightly constrained by both the latent heat
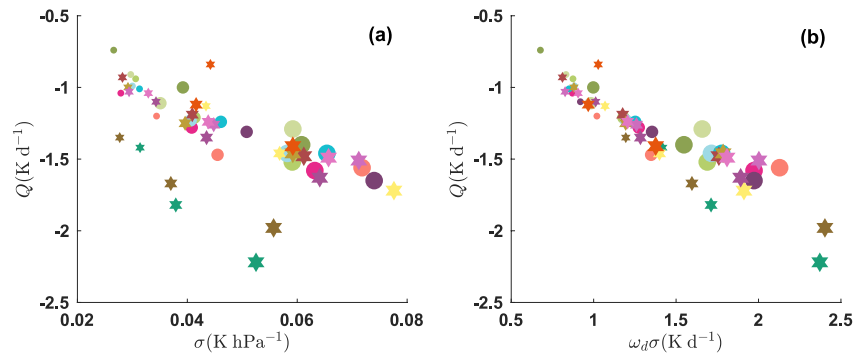
Figure 7. (a) Scatter plot of net radiative heating, Q, and the static stability, σ. (b) The static stability has been scaled by each model's mean ω_d. Vertical mass-weighted averages were taken between 600 and 200 hPa. Includes only the models which saved clear-sky fluxes. Circles (stars) indicate General Circulation Models (Cloud-system Resolving Models) and increasing marker size indicates increases values of T_s.

flux and the net atmospheric radiative cooling (e.g., Allen & Ingram, 2002; O'Gorman et al., 2012; Pendergrass & Hartmann, 2014), but the direction of causality between the latent heat flux and the atmospheric cooling in explaining the variability of P across models is difficult to determine. Jeevanjee and Romps (2018) derived an argument for the mean change of P based on the radiative constraint on P. Their argument is based in part on an invariance of radiative cooling profiles in temperature space. There is also evidence that low-level clouds have a strong influence on the radiative cooling profile in the lower troposphere and the consequent P (Jeevanjee & Romps, 2018; Silvers & Robinson, 2021; Watanabe et al., 2018). The large range of values that we see for PW is not constrained by the latent heat flux in any obvious way (Figure 6a) although it is known (both in simulations and observations) that increased convective aggregation leads to drier mean states (Bretherton et al., 2005; Holloway et al., 2017; Tobin et al., 2012; Wing et al., 2017). We hypothesize that the variability of PW among models is driven by differences in the strength of convective mixing, precipitation efficiency, and the state of convective aggregation.

4.2. Diagnosing the Range of the Diabatic Velocity and Relative Humidity

In this subsection we seek to better understand why there is a such a large range in the values of ω_d and RH among the RCEMIP models. We have shown that much of the variability of both I and $\Delta I/\Delta T_s$ is highly correlated with, and mirrors $\omega^\uparrow$ and $\Delta \omega^\uparrow/\Delta T_s$. Additionally, the physical processes of the clear-sky portions of the domain play a role in determining the tropical response to warming. Recall that the mean correlation of $\omega^\downarrow$ and ω_d among individual models is 0.94 (mean of last column in Table 2). Despite this high correlation, the particular values of ω_d cover a wide range (Figure 3). From Equation 2, ω_d is directly proportional to the clear-sky radiative cooling, Q, and inversely proportional to the static stability, σ. Static stability is essentially set by the lapse rate of temperature which thermodynamically connects the convective and clear-sky regions of the tropics. Thus ω_d, and by implication $\omega^\downarrow$, while characterizing the clear-sky regions of the tropics is also closely tied to the deep convection through the dependence of ω_d on the lapse rate of temperature and the RH that are strongly influenced by the deep convection.

To better understand the source of the large spread in ω_d that we find in the RCEMIP simulations, Figure 7 presents Q and σ from each simulation. Across the full ensemble of models and all T_s there is a range of $Q \sim 1.5$ K day^{-1} and $\sigma \sim 0.05$ K hPa^{-1}. For each particular T_s there is also substantial spread across the models of both Q (~ 1 K day^{-1}) and σ (~ 0.02 K hPa^{-1}) as shown in Figure 7a. To assist the comparison of the variability between Q and σ which naturally have different units, we use the mean of ω_d across the three T_s values for each particular model to scale σ for that particular model in Figure 7b. This reveals that both Q and the scaled σ have a range of ~ 1.5 K day^{-1}. We conclude that the spread in ω_d within the RCEMIP models is due to large variations in both Q and σ and is not dominated by either individually. However, the decrease of ω_d with warming that is apparent in Figures 3 and 4 is not due to the changes of Q, it is caused by the robust increase of σ as the surface is warmed (not shown).

Mapes (2001) showed that radiatively driven subsidence, or diabatic velocity, ω_d, drives the drying of the troposphere and leads to a "C" shaped RH profile. This profile has been noted in observations and discussed
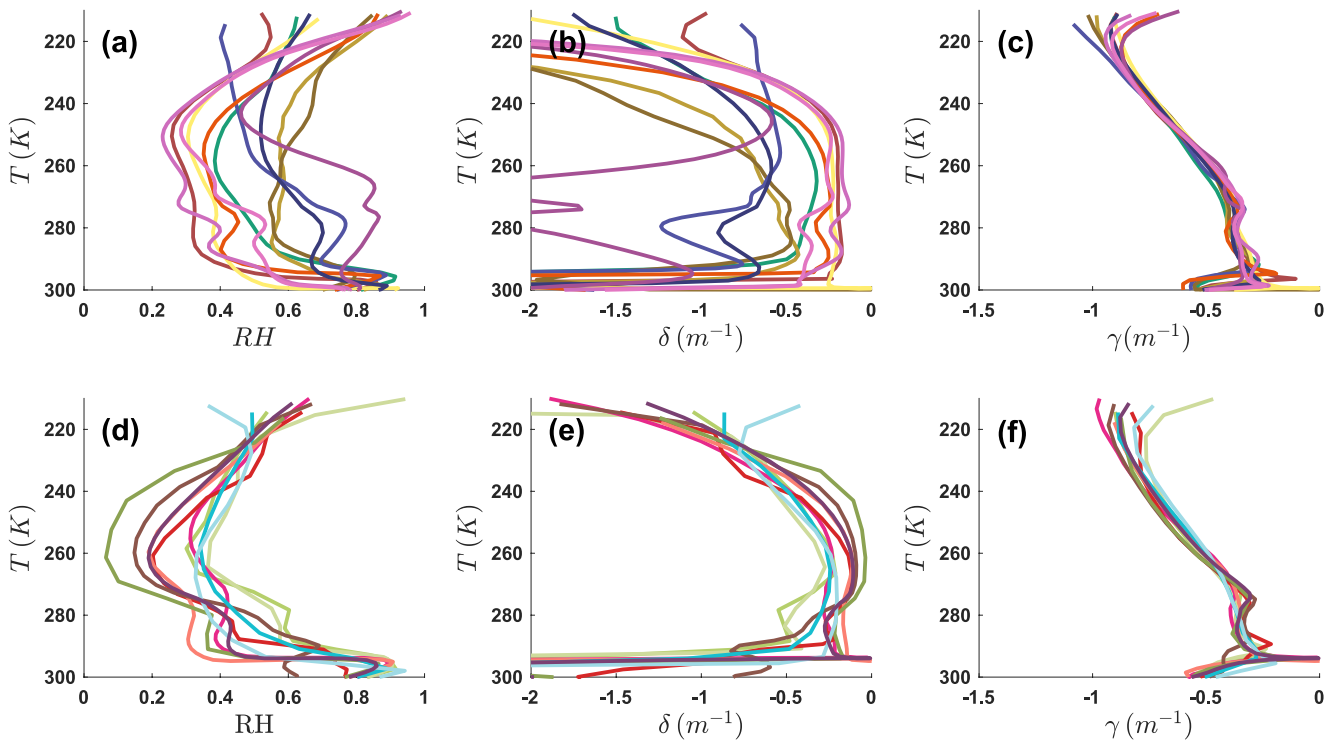
Figure 8. Relative Humidity (left), fractional convective detrainment, δ (middle), and water vapor lapse rate, γ (right). Panels a–c show Cloud-system Resolving Models and panels d–f show General Circulation Models. All panels show data from the radiative convective equilibrium simulation with an T_s of 305 K.

theoretically by Romps (2014). The relative humidity profiles in most of the RCEMIP models show the expected mid-tropospheric minimum of *RH* (Figures 8a and 8d) and the usual "C" shaped profile. We expect that the range of ω_d values seen in the RCEMIP models contribute to the enormous range ($\sim$15% − 85%) of mid-tropospheric *RH* profiles seen in Figures 8a and 8d. Although a large amount of variability in the *RH* sink term, ω_d, is apparent in Figures 3 and 4, ω_d is not highly correlated with the midtropospheric *RH* across the model ensemble (not shown). There must be an additional source of the variability in the *RH* profiles. Both Sherwood et al. (2006) and Romps (2014) argue that the steady state mean tropospheric humidity field is the result of a balance between the subsidence drying that is reflected in ω_d and moistening from convective detrainment. Assuming convection can be treated as a bulk plume having the same temperature as its environment and in which condensate precipitates out immediately after formation, Romps (2014) derived an analytic expression for this balance of moistening and drying:

$$RH = \frac{\delta}{\delta + \gamma} \tag{4}$$

in which δ is the fractional detrainment rate, γ is the lapse rate of water vapor, and it has been assumed that *RH* varies over larger characteristic distances than the saturation specific humidity. The lapse rate of water vapor can be written as a function of only temperature and the lapse rate of temperature (see Equation 6 of Romps (2014)). Assuming that Equation 4 is valid, we can calculate γ and diagnose inferred profiles of δ for each model based on the steady state *RH* and *T* in the RCE simulations. Importantly, this implied detrainment is not necessarily equivalent to the actual detrainment as measured from convection in the models given the many simplifying assumptions in Romps (2014). However, if we treat Equation 4 as a conceptual model for *RH*, we find that most of the range in *RH* profiles among models is reflected in the inferred δ profiles (Figures 8b and 8e) and that the water vapor lapse rate, γ, is quite consistent among the models (Figures 8c and 8f). A wide range of entrainment and detrainment rates are expected among the RCEMIP models. GCMs often specify the entrainment and detrainment in the convective parameterization schemes with one or more parameters. However, in CRMs which do not use convective parameterizations, the entrainment and detrainment are often emergent properties that are based on the resolved dynamics and the subgrid-scale turbulence parameterization scheme. Comparing the *RH* profiles

to the δ profiles offers support to the intuitive idea that models which detrain more moisture from the convective regions will have more moisture in the mean environment. Conversely, the models with the lowest midtropospheric *RH* values have the smallest amount of inferred detrainment.

The CRMs have a larger (relative to the GCMs) range of *RH* values in the mid-trosphere and a greater diversity of profile shapes, especially so for the 305 K simulation shown in Figure 8. Despite the large range of *RH* values, the *RH* profiles remain approximately constant for each model as the T_s increases (generally less than 5% K^{-1}; not shown). The GEOS model is an exception to this and has a large change of the *RH* between the 300 and 305 K simulations which could explain why the change of both M_{wv} and *I* is so different in GEOS relative to the majority of the other models (Figures 1b and 2a). Given the relatively tight constraints and consistent boundary conditions that the RCEMIP protocol dictated (Wing et al., 2018) it is remarkable how unconstrained the mid-tropospheric *RH* is among these 21 models. In addition to detrainment (Romps, 2014; Singh et al., 2019), *RH* may also be controlled by precipitation efficiency and downdrafts (Emanuel, 2019). If we consider the constraint on precipitation efficiency of PE $\geq 1 - RH$ derived by Romps (2014), this would imply a substantially higher PE in those models which have drier *RH* profiles. The feasibility of using simple theory to diagnose inferred values of PE and δ is the subject of ongoing work; here we simply point out that the *RH* profiles suggest a wide range of PE and δ values that could reflect the many varieties of subgrid-scale parameterizations employed by these 21 models.

Several "families" of models can be seen in Figure 8 to have profiles that group together, perhaps because of overlapping parameterizations. These include the WRF family (WRF-COL-CRM, WRF-CRM: dark blue-purple), the ICON family (ICON-LEM, ICON-NWP: tan-browns), the SP-CAM family (SP-CAM, SPX-CAM: blue-cyan), and the CAM family (CAM5-GCM, CAM6-GCM: light-greens). The UKMO-CRM family (UKMO-CASIM, UKMO-RA1-T, UKMO-RA1-T-nocloud: pink to violet) is a notable exception in which the family members prefer to occupy very different states. A few additional details are given in Appendix A.

5. Conclusions

Two distinct approaches have been used to quantify the large-scale overturning circulation and measure the change with surface warming. The first measure, the cycling rate of water vapor, M_{wv}, uses the ratio of the mean precipitation (*P*) and *PW* to infer the exchange of mass between the BL and the midtroposphere. The second measure, the intensity of the circulation, *I*, depends on the midtropospheric vertical velocity. A 21 member ensemble of models from the RCEMIP has been used to calculate the response of the large-scale atmospheric circulation to warming in the context of both global GCMs and large-domain CRMs, all simulating RCE. Robust responses to warming of the models include the following:

- The water vapor cycling rate decreases with increasing T_s ($\Delta M_{wv}/\Delta T_s < 0$) for all but one of the models.
- The intensity of the circulation decreases with increasing T_s ($\Delta I/\Delta T_s < 0$) for about 90% of the individual models.
- The large range of *I* and of $\Delta I/\Delta T_s$ are best explained by $\omega^{\uparrow}$ and $\Delta\omega^{\uparrow}/\Delta T_s$, respectively, across the full ensemble of models.
- The fractional change of the water vapor cycling rate ((ΔM_{wv})/M_{wv}), about -0.04 ± 0.01, is much more consistent among the models than the fractional change of the intensity of the circulation (ΔI)/*I*.
- The diabatic velocity, ω_d, decreases with increasing T_s ($\Delta\omega_d/\Delta T_s < 0$) in all models, driven by increasing static stability, σ.
- The downward velocity decreases with increasing T_s ($\Delta\omega^{\downarrow}/\Delta T_s < 0$) in all models.
- The static stability, σ, and the mean radiative cooling of the clear-sky regions, *Q*, both increase with warming.

These responses to warming illustrate the relevance of RCE simulations as a tool with which to study physical processes of the Earth's tropical regions. Some understanding of the response of the circulation and atmospheric stability to a warming surface was previously developed through the use of simple models (Betts & Ridgway, 1989), analysis of global climate models (Held & Soden, 2006; Knutson & Manabe, 1995; Medeiros et al., 2015; Vecchi & Soden, 2007), and the analysis of RCE simulations from a particular model (Bony et al., 2016; Cronin & Wing, 2017). The present study demonstrates how broadly applicable the basic physics of a decreasing circulation strength with warming is in simulations that use both GCMs and CRMs, adding confidence to our understanding.

The response of the large-scale tropical circulation to warming that we have illustrated with these results from RCEMIP demonstrates the interlocking relationships among many of the key variables. Increasing T_s leads to an

increased static stability, σ, and a correspondingly smaller diabatic velocity, ω_d. Warmer surface temperatures also lead to larger fluxes of latent heat from the surface and more domain mean precipitation which is eventually reflected in the net atmospheric cooling to space. The radiative cooling to space is strongly influenced by the distribution of clouds and the increased PW that is dictated by the CC relation. The utility of RCE simulations is confirmed by the fact that these same interlocking relationships act in the observed tropical atmosphere of Earth and in many comprehensive GCMs (Bony et al., 2016; Knutson & Manabe, 1995). For the calculation of ω_d the net diabatic heating in the regions of subsidence was approximated by the mean clear-sky radiative heating. This provides a test of how well the theoretical idealization of clear sky radiative-subsidence balance can predict descending motion across the range of RCEMIP models. This is valuable because the approximation is common in the literature (Bony et al., 2016; Cronin & Wing, 2017; Mapes, 2001; Stauffer & Wing, 2022; Thompson et al., 2017) and in theoretical models (e.g., Emanuel, 2019) but has not been broadly tested. Our results indicate that calculating ω_d with the domain mean clear-sky cooling rate is useful but that the particular relationship between ω_d and $\omega^{\downarrow}$ is model dependent.

One of the most interesting results of this multi-model comparison is the extent to which the equilibrated climate can still vary among models within the framework of this response to warming. The latent heat flux for example, is expected to increase with warming, but for individual models that increase can range from about 10 W m^{-2} K^{-1} to less than 1 W m^{-2} K^{-1}. Both the GCMs and the CRMs display similarly large ranges of variability among basic variables such as σ and PW. This confirms what has been known for years, that increased resolution alone will not eliminate the uncertainty that is present in our models. Although GCMs are sensitive to resolution (Herrington & Reed, 2020; Reed & Medeiros, 2016), a better understanding of the parameterized moist processes is essential. Simulations of RCE can facilitate tests of our process-level understanding of convective parameterizations and microphysics. Analysis of the RCEMIP simulations in the CAM5 and CAM6 GCMs has shown that major differences in the low-level clouds, which are in part due to differences in parameterized convection and BL processes, are also reflected in the tropical clouds of the parent models, CESM1 and CESM2 (Reed et al., 2021). Reed et al. (2021) also documented an official public release of the RCEMIP setup in CAM (QPRCEMIP) that should be used by the wider community for additional RCE studies.

Some of the previous studies that illustrated the weakening of the tropical circulation of coupled Earth-like global climate models in response to a warming climate (Knutson & Manabe, 1995; Vecchi & Soden, 2007) found that the Walker circulation was the component of the tropical overturning circulation that decreased in magnitude. The fact that RCE models of the tropical circulation with uniform T_s reproduce this change of circulation with warming implies that the change of circulation is not driven by changes in the pattern of T_s that is characteristic of the Walker Circulation, but rather due to basic physical processes of the atmosphere as argued by both Knutson and Manabe (1995) and Held and Soden (2006). Nevertheless, the wide range of variability we find in both the circulation and the change of circulation with warming could be partly due to an underconstrained system. Several previous studies (Cronin & Wing, 2017; Jeevanjee et al., 2017; Silvers & Robinson, 2021) have hypothesized that imposing a mock-Walker Circulation on models of RCE could help to increase the applicability of the results, relative to strict RCE. A mock-Walker circulation is probably the simplest way to incorporate forced large-scale circulations into the balance between radiation and convection and is one step closer to the observed tropical atmosphere. This would provide a potentially fruitful comparison between GCMs and CRMs. But more importantly, utilizing the mock-Walker circulation in an RCE-like setting would highlight interactions between the tropical circulations, radiation, and cloud systems in a context that should lead to a better understanding of the role that clouds play in Earth's climate.

Appendix A: Technical Notes on Specific RCEMIP Models

Many of the characteristics both of the large-scale circulation, and of tropical convection are dependent on the BL and the subcloud layer energy. The vertical and horizontal resolution of GCMs near the surface is therefore of interest as a possible difference of note between the models. The overview paper for initial RCEMIP results, (Wing et al., 2020) specified that the participating GCMs would employ the grids which they used for CMIP6. The result of this is that the GCMs in RCEMIP represent a wide range of vertical grids, with one model having only 26 vertical levels and another having 91. The horizontal resolutions are difficult to compare directly because of the different grids, but the grid spacing ranges from approximately 100 km to around 160 km. Of the 11 GCMs which participated in RCEMIP, 6 of them place the model level which is closest to the surface at 64 m (CAM5,

CAM6, SP-CAM, SPX-CAM, SAM-UNICON, and GEOS). The IPSL, ECHAM, and ICON models place their lowest level at 49, 33, and 20 m, respectively. The CNRM and UKMO GCMs both have the lowest model level at just 10 m above the surface. Initial findings (scatter plots not shown here) indicate that the height of the lowest atmospheric model level does not play a clear role in driving characteristics of the RCE experiments. It is well known that grid spacing in GCMs influences fundamental characteristics of the climate such as cloud distributions and the relative humidity (e.g., Herrington & Reed, 2020; Reed & Medeiros, 2016). An intercomparison of GCMs running RCE using the same grid would be useful.

Among the CRMs that completed simulations on the large domain there are a few "families" of models that share some components. The list below details this in extreme brevity, further specifications of RCEMIP models can be found in the Supporting Information of Wing et al. (2020).

- UKMO: The configurations of the UKMO-CASIM, UKMO-RA1-T and UKMO-RA1-T-nocloud are very similar to each other. UKMO-CASIM can be thought of as the base model. UKMO-RA1-T has different microphysics and uses a sub-grid cloud scheme. The UKMO-RA1-T-nocloud simply disable this sub-grid cloud scheme.
- WRF: WRF-COL-CRM and WRF-CRM are very different models. The radiation schemes, the microphysics, and the turbulence schemes all differ. However, they both uses double moment microphysics (but not the same scheme). They have the same BL scheme, but different sub-grid turbulence. The multiple ensembles of the WRF-GCM are based off of the WRF-COL-CRM model.
- ICON: The two ICON CRMs (ICON-LEM and ICON-NWP) use the same dynamical core, grid, parameterization of longwave and shortwave radiation (RRTMG), and two-moment mixed phase bulk microphysics scheme (Seifert & Beheng, 2006). The parameterizations for BL turbulence, subgrid-scale turbulence, and cloud cover differ.

Appendix B: Changes of Water Vapor With Warming According to the Clausius-Clapyron Relation

The Clausius-Clapeyron relation can be written as

$$\frac{de^*}{dT} = \frac{Le^*}{RT^2} \tag{B1}$$

where R is the gas constant for water, $e*$ is the saturation vapor pressure, L represents the latent heat of condensation and T is the temperature. Following Stephens (1990), this equation can be approximated as

$$e_0^* = 17.044 e^{a(T_s - 288)} \tag{B2}$$

in which T_s is the SST and $a \approx 0.064$ k^{-1}. Using Equation B2 Stephens then derives an approximate relationship between PW (PW, kg m^{-2}) and T_s as

$$PW = 108.2 \left(\frac{r}{1 + \lambda}\right) e^{a(T_s - 288)}. \tag{B3}$$

In Equation B3 r is the surface value of relative humidity and H/λ is the scale height of water vapor if H is the atmospheric scale height. Typical values of H and λ are 7 km and 3.5, respectively. The three black lines in the left panel of Figure 1 show Equation B3 plotted with three values of the coefficient $r/(1 + \lambda)$: 0.1, 0.15, and 0.2. The values of parameters and constants in Equations B1–B3 are all as in Stephens (1990).

Data Availability Statement

All official RCEMIP output is publicly available at http://hdl.handle.net/21.14101/d4beee8e-6996-453e-bbd1-ff53b6874c0e, hosted by the German Climate Computing Center (DKRZ).

References

Allen, M. R., & Ingram, W. J. (2002). Constraints on future changes in climate and the hydrologic cycle. *Nature*, *419*(6903), 228–232. https://doi.org/10.1038/nature01092

Betts, A. K., & Ridgway, W. (1989). Climatic equilibrium of the atmospheric convective boundary layer over a tropical ocean. *Journal of the Atmospheric Sciences*, *46*(17), 522–2641. https://doi.org/10.1175/1520-0469(1989)046⟨2621:CEOTAC⟩2.0.CO;2

Bjerknes, J. (1938). Saturated-adiabatic ascent of air through dry-adiabatically descending environment. *Quarterly Journal of the Royal Meteorological Society*, *64*, 325–330.

Boer, G. J. (1993). Climate change and the regulation of the surface moisture and energy budgets. *Climate Dynamics*, *8*(5), 225–239. https://doi.org/10.1007/BF00198617

Bony, S., Bellon, G., Klocke, D., Sherwood, S., Fermepin, S., & Denvil, S. (2013). Robust direct effect of carbon dioxide on tropical circulation and regional precipitation. *Nature Geoscience*, *6*(6), 447–451. https://doi.org/10.1038/ngeo1799

Bony, S., Dufresne, J. L., Treut, H. L., Morcrette, J.-J., & Senior, C. (2004). On dynamic and thermodynamic components of cloud changes. *Climate Dynamics*, *22*(2–3), 71–86. https://doi.org/10.1007/s00382-003-0369-6

Bony, S., & Stevens, B. (2020). Clouds and warming. In A. P. Siebesma, S. Bony, C. Jakob, & B. Stevens (Eds.), *Clouds and climate* (pp. 356–388). Cambridge University Press.

Bony, S., Stevens, B., Coppin, D., Becker, T., Reed, K. A., Voigt, A., & Medeiros, B. (2016). Thermodynamic control of anvil cloud amount. *Proceedings of the National Academy of Sciences of the United States of America*, *113*(32), 8927–8932. https://doi.org/10.1073/pnas.1601472113

Bosilovich, M. G., Schubert, S. D., & Walker, G. K. (2005). Global changes in water cycle intensity. *Journal of Climate*, *18*(10), 1591–1608. https://doi.org/10.1175/JCLI3357.1

Bretherton, C. S., Blossey, P. N., & Khairoutdinov, M. (2005). An energy-balance analysis of deep convective self-aggregation above uniform SST. *Journal of the Atmospheric Sciences*, *62*(12), 4273–4292. https://doi.org/10.1175/jas3614.1

Bretherton, C. S., & Sobel, A. H. (2002). A simple model of a convectively coupled walker circulation using the weak temperature gradient approximation. *Journal of Climate*, *15*(20), 2907–2920. https://doi.org/10.1175/1520-0442(2002)015⟨2907:ASMOAC⟩2.0.CO;2

Charney, J. G. (1963). A note on large-scale motions in the tropics. *Journal of the Atmospheric Sciences*, *20*(9), 607–609. https://doi.org/10.1175/1520-0469(1963)020⟨0607:ANOLSM⟩2.0.CO;2

Coppin, D., & Bony, S. (2015). Physical mechanisms controlling the initiation of convective self-aggregation in a general circulation model. *Journal of Advances in Modeling Earth Systems*, *7*(4), 2060–2078. https://doi.org/10.1002/2015MS000571

Cronin, T. W., & Wing, A. A. (2017). Clouds, circulation, and climate sensitivity in a radiative-convective equilibrium channel model. *Journal of Advances in Modeling Earth Systems*, *9*(8), 2883–2905. https://doi.org/10.1002/2017MS001111

Emanuel, K. (2019). Inferences from simple models of slow, convectively coupled processes. *Journal of the Atmospheric Sciences*, *76*(1), 195–208. https://doi.org/10.1175/JAS-D-18-0090.1

Flaschner, D., Mauritsen, T., & Stevens, B. (2016). Understanding the intermodel spread in global-mean hydrological sensitivity. *Journal of Climate*, *29*(1), 801–817. https://doi.org/10.1175/JCLI-D-15-0351.1

Grabowski, W. W., Yano, J.-I., & Moncrieff, M. W. (2000). Cloud resolving modeling of tropical circulations driven by large-scale SST gradients. *Journal of the Atmospheric Sciences*, *57*(13), 2022–2040. https://doi.org/10.1175/1520-0469(2000)057⟨2022:CRMOTC⟩2.0.CO;2

Held, I. M., & Soden, B. J. (2006). Robust responses of the hydrological cycle to global warming. *Journal of Climate*, *19*(21), 5686–5699. https://doi.org/10.1175/JCLI3990.1

Herrington, A. R., & Reed, K. A. (2020). On resolution sensitivity in the community atmospheric model. *Quarterly Journal of the Royal Meteorological Society*, *146*(733), 3789–3807. https://doi.org/10.1002/qj.3873

Holloway, C. E., Wing, A. A., Bony, S., Muller, C., Masunaga, H., L'Ecuyer, T. S., et al. (2017). Observing convective aggregation. *Surveys in Geophysics*, *38*(6), 1199–1236. https://doi.org/10.1007/s10712-017-9419-1

Jeevanjee, N., Hassanzadeh, P., Hill, S., & Sheshadri, A. (2017). A perspective on climate model hierarchies. *Journal of Advances in Modeling Earth Systems*, *9*(4), 1760–1771. https://doi.org/10.1002/2017MS001038

Jeevanjee, N., & Romps, D. M. (2018). Mean precipitation change from a deepening troposphere. *Proceedings of the National Academy of Sciences of the United States of America*, *115*(45), 11465–11470. https://doi.org/10.1073/pnas.1720683115

Jenney, A., Randall, D., & Branson, M. (2020). Understanding the response of tropical ascent to warming using an energy balance framework. *Journal of Advances in Modeling Earth Systems*, *12*(6), e2020MS002056. https://doi.org/10.1029/2020MS002056

Knutson, T. R., & Manabe, S. (1995). Time-mean response over the tropical Pacific to increased c02 in a coupled ocean-atmosphere model. *Journal of Climate*, *8*(9), 2181–2199. https://doi.org/10.1175/1520-0442(1995)008⟨2181:TMROTT⟩2.0.CO;2

Larson, K., Hartmann, D. L., & Klein, S. A. (1999). The role of clouds, water vapor, circulation, and boundary layer structure in the sensitivity of the tropical climate. *Journal of Climate*, *12*(8), 2359–2374. https://doi.org/10.1175/1520-0442(1999)012⟨2359:TROCWV⟩2.0.CO;2

Lutsko, N. J., & Cronin, T. W. (2018). Increase in precipitation efficiency with surface warming in radiative-convective equilibrium. *Journal of Advances in Modeling Earth Systems*, *10*(11), 2992–3010. https://doi.org/10.1029/2018MS001482

Mackie, A., & Byrne, M. (2021). Effects of circulation on tropical cloud feedbacks in high-resolution simulations. *ESS Open Archive*. https://doi.org/10.1002/essoar.10509780.1

Mapes, B. (2001). Water's two height scales: The moist adiabat and the radiative troposphere. *Quarterly Journal of the Royal Meteorological Society*, *127*(577), 2353–2366. https://doi.org/10.1002/qj.49712757708

Medeiros, B., Stevens, B., & Bony, S. (2015). Using aquaplanets to understand the robust responses of comprehensive climate models to forcing. *Climate Dynamics*, *44*(7–8), 1957–1977. https://doi.org/10.1007/s00382-014-2138-0

O'Gorman, P. A., Allan, R. P., Byrne, M., & Previdi, M. (2012). Energetic constraints on precipitation under climate change. *Surveys in Geophysics*, *33*(3–4), 585–608. https://doi.org/10.1007/s10712-011-9159-6

O'Gorman, P. A., & Muller, C. J. (2010). How closely do changes in surface and column water vapor follow Clausius-Clapeyron scaling in climate simulations? *Environmental Research Letters*, *5*(2), 025207. https://doi.org/10.1088/1748-9326/5/2/025207

Pendergrass, A. G., & Hartmann, D. L. (2014). The atmospheric energy constraint on global-mean precipitation change. *Journal of Climate*, *27*(2), 757–768. https://doi.org/10.1175/JCLI-D-13-00163.1

Randall, D. (2015). *An introduction to the global circulation of the atmosphere* (1st ed.). Princeton University Press.

Raymond, D. J. (1994). Convective processes and tropical atmospheric circulations. *Quarterly Journal of the Royal Meteorological Society*, *120*(520), 1431–1455. https://doi.org/10.1002/qj.49712052002

Reed, K. A., & Medeiros, B. (2016). A reduced complexity framework to bridge the gap between AGCMs and cloud-resolving models. *Geophysical Research Letters*, *43*(2), 860–866. https://doi.org/10.1002/2015GL066713

Reed, K. A., Silvers, L. G., Wing, A. A., Hu, I.-K., & Medeiros, B. (2021). Using radiative convective equilibrium to explore clouds and climate in the Community Atmosphere Model. *Journal of Advances in Modeling Earth Systems*, *13*(12), e2021MS002539. https://doi.org/10.1029/2021MS002539

Rieck, M., Nuijens, L., & Stevens, B. (2012). Marine boundary layer cloud feedbacks in a constant relative humidity atmosphere. *Journal of the Atmospheric Sciences*, *69*(8), 2538–2550. https://doi.org/10.1175/jas-d-11-0203.1

Riehl, H., & Malkus, J. (1958). On the heat balance in the equatorial trough zone. *Geophysica*, *6*, 503–538.

Roads, J., Chen, S., Marshall, S., & Oglesby, R. (1998). Atmospheric moisture cycling rates. *GEWEX News*, *8*, 7–10.

Romps, D. M. (2014). An analytical model for tropical relative humidity. *Journal of Climate*, *27*(19), 7432–7449. https://doi.org/10.1175/jcli-d-14-00255.1

Seifert, A., & Beheng, K. (2006). A two-moment cloud microphysics parameterization for mixed-phase clouds. Part 1: Model description. *Meteorology and Atmospheric Physics*, *92*(1–2), 45–66. https://doi.org/10.1007/s00703-005-0112-4

Shepherd, T. G. (2014). Atmospheric circulation as a source of uncertainty in climate change projections. *Nature Geoscience*, *7*(10), 703–708. https://doi.org/10.1038/ngeo2253

Sherwood, S. C., Kursinski, E. R., & Read, W. G. (2006). A distribution law for free-tropospheric relative humidity. *Journal of Climate*, *19*(24), 6267–6277. https://doi.org/10.1175/JCLI3978.1

Sherwood, S. C., Webb, M. J., Annan, J. D., Armour, K. C., Forster, P. M., Hargreaves, J. C., et al. (2020). An assessment of Earth's climate sensitivity using multiple lines of evidence. *Reviews of Geophysics*, *58*(4), e2019RG000678. https://doi.org/10.1029/2019RG000678

Silvers, L. G., & Robinson, T. (2021). Clouds and radiation in a mock-walker circulation. *Journal of Advances in Modeling Earth Systems*, *13*(2), e2020MS002196. https://doi.org/10.1029/2020MS002196

Singh, M. S., Warren, R. A., & Jakob, C. (2019). A steady-state model for the relationship between humidity, instability, and precipitation in the tropics. *Journal of Advances in Modeling Earth Systems*, *11*(12), 3973–3994. https://doi.org/10.1029/2019MS001686

Sobel, A. H., Nilsson, J., & Polvani, L. M. (2001). The weak temperature gradient approximation and balanced tropical moisture waves. *Journal of the Atmospheric Sciences*, *58*(23), 3650–3665. https://doi.org/10.1175/1520-0469(2001)058⟨3650:TWTGAA⟩2.0.CO;2

Stauffer, C. L., & Wing, A. A. (2022). Properties, changes, and controls of deep-convective clouds in Radiative-Convective Equilibrium. *Journal of Advances in Modeling Earth Systems*, *14*(6), e2021MS002917. https://doi.org/10.1029/2021MS002917

Stephens, G. L. (1990). On the relationship between water vapor over the oceans and sea surface temperature. *Journal of Climate*, *3*(6), 634–645. https://doi.org/10.1175/1520-0442(1990)003⟨0634:OTRBWV⟩2.0.CO;2

Thompson, D. W. J., Bony, S., & Li, Y. (2017). Thermodynamic constraint on the depth of the global tropospheric circulation. *Proceedings of the National Academy of Sciences of the United States of America*, *114*(31), 8181–8186. https://doi.org/10.1073/pnas.1620493114

Tobin, I., Bony, S., & Roca, R. (2012). Observational evidence for relationships between the degree of aggregation of deep convection, water vapor, surface fluxes, and radiation. *Journal of Climate*, *25*(20), 6885–6904. https://doi.org/10.1175/jcli-d-11-00258.1

Tompkins, A. M. (2001). On the relationship between tropical convection and sea surface temperature. *Journal of Climate*, *14*(5), 633–637. https://doi.org/10.1175/1520-0442(2001)014⟨0633:OTRBTC⟩2.0.CO;2

Vecchi, G. A., & Soden, B. J. (2007). Global warming and the weakening of the tropical circulation. *Journal of Climate*, *20*(17), 4316–4340. https://doi.org/10.1175/JCLI4258.1

Voigt, A., & Shaw, T. A. (2015). Circulation response to warming shaped by radiative changes of clouds and water vapour. *Nature Geoscience*, *8*(2), 102–106. https://doi.org/10.1038/ngeo2345

Watanabe, M., Kamae, Y., Shiogama, H., DeAngelis, A. M., & Suzuki, K. (2018). Low clouds link equilibrium climate sensitivity to hydrological sensitivity. *NatCC*, *8*(10), 901–907. https://doi.org/10.1038/s41558-018-0272-0

Wing, A. A., Emanuel, K., Holloway, C. E., & Muller, C. (2017). Convective self-aggregation in numerical simulations: A review. *Surveys in Geophysics*, *38*(6), 1173–1197. https://doi.org/10.1007/s10712-017-9408-4

Wing, A. A., Reed, K. A., Satoh, M., Stevens, B., Bony, S., & Ohno, T. (2018). Radiative–convective equilibrium model intercomparison project. *Geoscientific Model Development*, *11*(2), 793–813. https://doi.org/10.5194/gmd-11-793-2018

Wing, A. A., Stauffer, C. L., Becker, T., Reed, K. A., Ahn, M.-S., Arnold, N. P., et al. (2020). Clouds and convective self-aggregation in a multi-model ensemble of radiative-convective equilibrium simulations. *Journal of Advances in Modeling Earth Systems*, *12*(9), e2020MS002138. https://doi.org/10.1029/2020MS002138